International Journal of Applied Earth Observation and Geoinformation 137 (2025) 104427

Contents lists available at ScienceDirect

International Journal of Applied Earth Observation and Geoinformation

journal homepage: www.elsevier.com/locate/jag

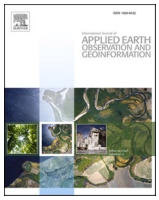

Expanding high-resolution sea surface salinity estimation from coastal seas to open oceans through the synergistic use of multi-source data with machine learning

Taejun Sung [a,1], So-Hyun Kim [a,1], Seongmun Sim [b], Daehyeon Han [c], Eunna Jang [d], Jungho Im [a,e,f,*]

[a] Department of Civil, Urban, Earth, and Environmental Engineering, Ulsan National Institute of Science and Technology (UNIST), Ulsan, Republic of Korea
[b] Nara Space Technology Inc., Seoul, Republic of Korea
[c] Department of Geography, University of Colorado Boulder, Boulder, CO, USA
[d] Korea Ocean Satellite Center, Korea Institute of Ocean Science and Technology, Busan, Republic of Korea
[e] Graduate School of Artificial Intelligence, UNIST, Ulsan, Republic of Korea
[f] Graduate School of Carbon Neutrality, UNIST, Ulsan, Republic of Korea

ARTICLE INFO

Keywords:
Sea surface salinity
Cold-water mass
Changjiang Diluted Water
SMAP
GOCI
HYCOM
Machine learning

ABSTRACT

High-spatiotemporal-resolution sea surface salinity (SSS) estimations are essential for understanding marine phenomena in both coastal seas and open oceans. Although studies have enhanced the resolution of SSS estimations using ocean color (OC) satellite data, the limited variance of OC signals and weak correlation with SSS in open oceans have confined these advancements to coastal seas. To overcome this limitation and broaden the scope of research, a machine learning-based approach is proposed that combines multi-source data. Geostationary Ocean Color Imager (GOCI) remote sensing reflectance (Rrs) was used as an input variable for a multilayer perceptron (MLP) model along with Hybrid Coordinate Ocean Model (HYCOM) SSS and multi-scale ultra-high-resolution sea surface temperature (MURSST) to simulate corrected and gap-filled Soil Moisture Active Passive (SMAP) SSS for East Asia. The high-quality SSS data generated by the proposed approach, with fine spatial (500–m) and temporal (hourly) resolutions, simulated detailed seasonal and spatial variations in SSS across both coastal seas and open oceans. In validation with in situ observations, the MLP model performed better than SMAP, achieving an R^2 of 0.80 and an RMSE of 0.92 psu, whereas SMAP achieved an R^2 of 0.76 and an RMSE of 1.05 psu. Shapley additive explanations analysis revealed that the contributions of input variables to SSS estimations varied by region and season. In the open ocean, HYCOM SSS and MURSST made significant contributions, compensating for the weaker relationship with Rrs. In coastal areas, Rrs412 and Rrs555 showed a positive correlation with SSS. This integration enabled the detection of high-resolution SSS, including changes driven by cold-water masses near the coastline of the East Sea. The findings of this study advance the generation of high-resolution SSS data for East Asia and also enhance our understanding of the relationship between OC properties and SSS.

1. Introduction

Sea surface salinity (SSS) is a critical climatic variable, as identified by the World Meteorological Organization. It determines the density of seawater, influences both surface and deep ocean circulation, and serves as a tracer for processes such as evapotranspiration, river runoff, ice formation, and melting (Barale et al., 2010; Martin, 2014). The influx of low-salinity water from river discharge can significantly alter marine ecosystems and harm aquaculture species (Choi et al., 2021; Son and Choi, 2022). Continuous and extensive observations of SSS are crucial for enhancing our understanding of ocean circulation and mitigating the effects of low-salinity water at global and regional scales. However, although several in situ platforms, such as the Argo project, have been developed since the early 2000 s, they suffer from limited

* Corresponding author.
E-mail address: ersgis@unist.ac.kr (J. Im).
[1] The first two authors contributed equally to the paper.

https://doi.org/10.1016/j.jag.2025.104427
Received 31 October 2024; Received in revised form 1 January 2025; Accepted 12 February 2025
Available online 15 February 2025

spatiotemporal coverage.

L-band (1.4-GHz) passive microwave (PM) sensors have been used for global SSS monitoring. In this respect, the Soil Moisture and Ocean Salinity (SMOS) and the Soil Moisture Active Passive (SMAP) mission have been providing global SSS products since 2009 and 2015, respectively. PM SSS is viable because salinity and temperature influence the dielectric properties of seawater, affecting microwave emissions from the ocean surface (Klein and Swift, 1977; Stogryn, 1971). However, due to the low intensity of microwave radiance from the sea surface, PM SSS generally has a low spatial resolution to maintain accuracy. SMOS and SMAP offer data with spatial resolutions of 0.25–1° and a temporal resolution of three days or more, making them unsuitable for observing detailed spatiotemporal variations in SSS on a regional scale (Chen and Hu, 2017; Qing et al., 2013; Son and Choi, 2022). Additionally, L-band sensors are prone to land contamination (LC) and radio frequency interference (RFI), resulting in high uncertainty in coastal areas (Jang et al., 2021; Kim et al., 2023a; Kim et al., 2023b).

As an alternative to PM SSS, many studies have employed ocean color (OC) sensors for detailed monitoring of low-salinity waters in coastal seas (Chen and Hu, 2017; Jin et al., 2021; Qing et al., 2013; Shi and Wang, 2024). In East Asia, low-salinity waters have been monitored using the Geostationary Ocean Color Imager (GOCI) series (GOCI-I/II), which provides hourly OC information at a spatial resolution of 250–500 m (Choi et al., 2021; Kim et al., 2022; Kim et al., 2020). Optically sensitive parameters (OSPs), such as total suspended matter (TSM) and colored dissolved organic matter (CDOM), are correlated with SSS (Bai et al., 2013; Choi et al., 2021; Kim et al., 2009). However, the correlation between OSPs and SSS is limited to river-dominated areas, and it exhibits spatiotemporal variability due to local river characteristics and seasonality (Fournier et al., 2015; Kim et al., 2020). Several studies have used auxiliary variables, such as geolocation (longitude and latitude) and sea surface temperature (SST), to address the indirect correlation between OSPs and SSS (Chen and Hu, 2017; Kim et al., 2020). Nevertheless, most studies have focused on highly localized study areas, and their methods have not been extensively applied or tested in open oceans (Jin et al., 2021; Kim et al., 2009; Qing et al., 2013). Furthermore, while many studies have used data-driven techniques, such as machine learning, they have not sufficiently analyzed the contribution of input variables and their correlation with SSS (Chen and Hu, 2017; Kim et al., 2022).

In addition to satellite data, efforts have been made to extend the spatiotemporal coverage of in situ data. Ocean general circulation models combine long-term in situ observations with data assimilation techniques and physical equations to provide high-resolution salinity data. The hybrid coordinate ocean model (HYCOM) is a real-time, eddy-resolving ocean hindcast, nowcast, and prediction system developed at global and basin scales as part of the Global Ocean Data Assimilation Experiment (GODAE) (Chassignet et al., 2007). HYCOM offers high-resolution (4–8 km) information regarding boundary conditions on a regional scale and has potential applications in various coastal areas (Dorfschäfer et al., 2020; Zamudio et al., 2011). However, as HYCOM SSS relies on reference climatology in regions without global in situ platform data, it performs poorly in simulating low-salinity water in river-dominated areas (Jang et al., 2021; Wilson and Riser, 2016). While HYCOM SSS is highly accurate in open oceans with available in situ data, OC signals have a high correlation with SSS in river-dominated areas. Given that HYCOM SSS data exhibit spatial characteristics opposite those of OC signals, the two datasets are expected to complement each other when used together.

Many SSS estimation studies using OC satellite data have applied machine learning techniques to model the complex nonlinear relationships between SSS and OC signals (Chen and Hu, 2017; Kim et al., 2022; Kim et al., 2020). Machine learning approaches have shown higher accuracy than traditional statistical regression models; however, they are often viewed as black boxes due to their lack of interpretability. Explainable artificial intelligence (XAI) techniques have been developed to interpret these black box models, and they are useful for understanding the correlation and contribution between independent and dependent variables. Shapley additive explanations (SHAP) are among the most widely used XAI techniques used to interpret machine learning models and identify relationships between features. SHAP can provide insights into the complex spatiotemporal correlations between OC signals and SSS, while also analyzing potential error sources in OC satellite-based SSS estimation models.

Despite the significant advancements in SSS monitoring through the use of OC satellites, challenges remain, as current methods are restricted to localized areas and they are not sufficiently capable of analyzing the contributions of input variables to SSS. This study thus sought to bridge these gaps by using XAI techniques to integrate OC satellite data with SST and HYCOM data. Our objectives were to enhance the accuracy and interpretability of SSS estimation models across various spatial scales and provide a more comprehensive understanding of the underlying mechanisms and potential sources of error. By leveraging the complementary strengths of multi-source data, this study offers a novel approach for improving SSS monitoring, particularly in complex coastal seas and open oceans.

2. Study area and data

2.1. Study area

The study area encompasses East Asia (25–45°N, 120–140°E), which includes the East China Sea (ECS), East Sea (ES), Yellow Sea (YS), and Northwestern Pacific (NWP) (Fig. 1). This region covers both coastal seas and open oceans, exhibiting diverse salinity conditions. Coastal seas, such as the ECS and YS, experience low-salinity due to freshwater influx from Changjiang River discharge. The Changjiang Diluted Water (CDW) produces strong stratification and releases TSM and CDOM near the coast (Ahn et al., 2008; Yoon et al., 2004). In the ES, interactions between the North Korea Cold Current and East Korea Warm Current forms a subpolar front. In summer, strong southerly winds often cause upwelling along the ES coast, pushing coastal waters offshore and upwelling nutrient-rich, cold, salty bottom waters to the surface, forming a cold-water mass (Han et al., 2016; Kim et al., 2008).

2.2. In situ data

Thermosalinograph (TSG)-based global in situ SSS data for the ES and NWP were obtained from the Coriolis data center (https://www.coriolis.eu.org/). Coriolis provides oceanographic observations from various in situ platforms, including expendable bathythermographs (XBT), Argo, moored buoys, and TSG. TSG is a ship-based observation collected as part of the global ocean surface underway data program, providing numerous observations in nearshore regions among the in situ platforms available at Coriolis. In this study, only data marked as being of a good or probably good quality, with an observation depth of $\leq$ 5 m (1,957 samples) were used (Jang et al., 2022; Kolodziejczyk et al., 2021).

The National Institute of Fisheries Science (NIFS) provides in situ SSS data from Fishery Environment Monitoring (FEM) and the Serial Oceanographic Observations (SOO) program. The FEM monitors 261 stations at major aquaculture sites across South Korea four times a year to detect changes in coastal seas, particularly near estuaries (https://www.nifs.go.kr/femo/main.femo). The SOO monitors 207 stations across major South Korean seas (East Sea, South Sea, East China Sea, and Yellow Sea) four to six times a year to provide seasonal and regional comparisons of hydrographic and oceanographic conditions (https://www.nifs.go.kr/kodc/index.kodc). Only surface observation data (6,168 and 2,869 samples for FEM and SOO, respectively) were used in the analyses conducted here.

Publicly available in situ data around the Changjiang Estuary and the inner shelf of the ECS (24–33° N, 120–130° E) are limited. However, Liu

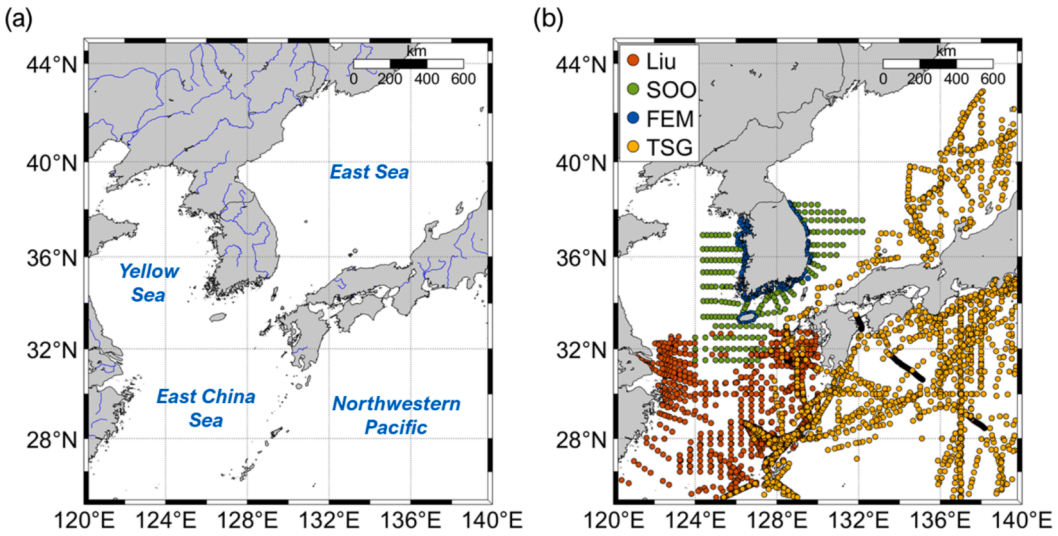

Fig. 1. (a) Entire study area (East Asia), including the four major seas (East China Sea, East Sea, Yellow Sea, and Northwestern Pacific). (b) The spatial distribution of in situ data provided from different sources. In situ data provided by Liu et al. (2023); serial oceanographic observation (SOO) and fishery environment monitoring (FEM) data provided by the National Institute of Fisheries Science; and thermosalinograph data (TSG) provided by Coriolis.

et al. (2023) provided publicly available in situ SSS data with a wide salinity range (0.1 to 35.44 psu) for the ECS, including the aforementioned regions, from 2003 to 2020. In situ SSS data were collected from local ship-based observations and global projects, including the World Ocean Database (WOD) and Surface Ocean CO_2 Atlas (SOCAT). From these data, 4,638 samples matching the satellite data during the study period were selected for evaluation (Fig. 1 for the spatial distribution of the in situ data).

2.3. Satellite data

The Jet Propulsion Laboratory (JPL) provides the SMAP Level 3 (L3) SSS version 5.0 dataset, with a daily temporal and 0.25° spatial resolution, via the National Aeronautics and Space Administration (NASA) Physical Oceanography Distributed Active Archive Center (PODAAC) (https://podaac.jpl.nasa.gov/). The gap-filled L3 product is generated by applying a Gaussian weighting of ± 3.5 days to the L2B product, derived from the combined active/passive (CAP) retrieval algorithm (Fore et al., 2016). However, the SMAP L2B product has low accuracy under certain conditions (i.e., RFI/LC, low sea surface temperature, strong winds, and heavy precipitation), as well as for the L3 product (Jang et al., 2024; Jang et al., 2022). Jang et al. (2022) improved the accuracy of SMAP L2B SSS by integrating SMAP and HYCOM data using a gradient-boosted regression tree model. Jang et al. (2024) applied the U-net model to produce gap-filled daily SSS with higher accuracy than the SMAP L3 SSS. The SMAP SSS corrected and gap-filled by Jang et al. (2024, 2022) (hereinafter, SMAP SSS-J) was used as a reference for the model training and validation.

The Korea Ocean Satellite Center (KOSC) provides GOCI L1B data through its website (https://kosc.kiost.ac.kr/). GOCI, the world's first geostationary ocean color sensor, was launched in 2010 aboard the Communication, Ocean, and Meteorological Satellite (COMS). For near-real-time monitoring of marine ecosystems, GOCI observes the East Asia region centered on the Korean Peninsula eight times a day from UTC 00:00 to 07:00 at a 500 m spatial resolution. It includes six visible bands (412, 443, 490, 555, 660, and 680 nm) for ocean color information and two near-infrared bands (745 and 865 nm) for atmospheric correction. In this study, remote sensing reflectance (Rrs) in six visible bands was used to estimate SSS.

Multi-scale ultra-high-resolution SST (MURSST) is a global SST analysis product provided daily at a spatial resolution of 0.01° × 0.01° by the Group for High Resolution SST (GHRSST) (Chin et al., 2017). MURSST was retrieved using a multi-resolution variational analysis that merged infrared-based (e.g., AVHRR and MODIS), microwave-based (e.g., AMSR-E, AMSR2, and WindSAT), and in situ SST (e.g., drifting and moored buoys) data (Woo and Park, 2020). The diurnal warming effect was removed using nighttime SST data, and the MURSST product is widely accepted among similar spatial resolution products (Woo and Park, 2020). In this study, MURSST was used to simulate the seasonal pattern of SSS, and level 4 version 4.1 products were downloaded from NASA PODAAC.

2.4. Numerical model data

HYCOM assimilates various satellite and in situ data (e.g., Argo, XBT, mooring buoys, and satellite altimeters) using the three-dimensional variational approach of the Navy-coupled Ocean Data Assimilation System (Chassignet et al., 2007; Cummings and Smedstad, 2013). HYCOM provides multiple versions of experimental data related to general ocean circulation (https://www.hycom.org/). This study used the standard field salinity (0 m depth) from the global ocean forecasting system version 3.1, with a 3-h temporal and 0.08° spatial resolution. To complement weak OC signals in the open ocean, HYCOM SSS was used to simulate moderate-to-high salinity.

Table 1 provides detailed information about the in situ, satellite, and numerical model data utilized in this study. Geolocation (latitude and longitude) were included as input to account for the specific characteristics of each sea in the study area.

3. Methods

This study aimed to accurately estimate high-resolution SSS in both coastal seas and open oceans using multi-source data and a multilayer perceptron (MLP) model (Fig. 2). In the data preprocessing phase, all input variables were resampled to match the spatiotemporal resolution of SMAP SSS-J for model training and GOCI Rrs for result estimation. During the model training phase, the MLP model learned the correlation between the independent variables (GOCI Rrs, MURSST, and HYCOM SSS) and the dependent variable (SMAP SSS-J). In the result estimation phase, the pre-trained MLP model generated high-resolution SSS using high-resolution input variables. The estimated SSS was validated using the holdout dataset (SMAP SSS-J) and further validated with an in situ dataset. SHAP was subsequently applied to examine the spatiotemporal relationships between the input variables and SSS. Finally, a cold-water

Table 1
Summary of data utilized in this study.

Type	Abbreviations	Description	Spatial resolution	Temporal resolution
In situ	TSG SSS	Sea surface salinity measured using a thermosalinograph	–	–
	FEM SSS	Sea surface salinity from Fishery Environment Monitoring	–	3 months
	SOO SSS	Sea surface salinity from Serial Oceanographic Observation	–	2–3 months
	Liu SSS	Sea surface salinity from Liu et al. (2023)	–	–
Satellite	SMAP L3 SSS	Level 3 sea surface salinity product from Soil Moisture Active Passive	0.25°	1 day
	SMAP SSS-J	Corrected and gap-filled SMAP Level 2B SSS by Jang et al. (2024, 2022)		
	GOCI Rrs412 GOCI Rrs443 GOCI Rrs490 GOCI Rrs555 GOCI Rrs660 GOCI Rrs680	Remote sensing reflectance at center wavelengths of 412, 443, 490, 555, 660, and 680 nm from Geostationary Ocean Color Imager	500 *m*	1 h
	MURSST	Multi-scale ultra-high-resolution sea surface temperature from Group for High-Resolution Sea Surface Temperature	0.01°	1 day
Numerical model	HYCOM SSS	Sea surface salinity from Hybrid Coordinate Ocean Model	0.08°	3 h
Geolocation	Latitude Longitude	– –	– –	– –

mass in the ES was analyzed using the derived high-resolution SSS.

3.1. Data preprocessing

The GOCI L1B radiance was converted to L2A Rrs using the GOCI data processing system version 2.0. The KOSC standard atmospheric correction algorithm was applied, and pixels with negative Rrs values were subsequently removed. Additionally, the quality assurance (QA) algorithm proposed by Wei et al. (2016) was applied to remove pixels with abnormal Rrs spectra, scoring satellite Rrs from 0 to 1 based on spectral similarity to a reference in situ Rrs. Pixels with a QA score of $<$ 0.5 were considered abnormal and removed (Kim et al., 2020).

The SMAP SSS-J, used as the reference data in model training, had the same spatiotemporal resolution as the SMAP L3 SSS (daily, 25 km). However, the output product from the trained model had the same spatiotemporal resolution as the GOCI Rrs (hourly, 500 m). Therefore, during the model training phase, each input variable was resampled to a daily 25 km resolution, while the original spatiotemporal resolution of GOCI Rrs was retained for the result estimation phase (Fig. 2). Bilinear interpolation was applied for spatial resampling. For temporal resampling, averaging and nearest neighbor matching were applied to the model training and result estimation phase, respectively.

When matching in situ and satellite data, different criteria were applied to account for their different spatiotemporal resolutions. In situ samples within 12.5 km from the SMAP data location on the same observation day were matched. Similarly, in situ samples were matched within 250 m of the GOCI data location and within 30 min of the GOCI observation time. When multiple in situ samples existed within a single satellite pixel, the average value was used.

3.2. Machine learning

The MLP model is an artificial intelligence tool commonly used for various regression and classification tasks. The MLP consists of three types of layers—input, hidden, and output—each containing multiple nodes. These nodes are interconnected and trained to determine the optimal weights and biases through feed-forward and back-propagation processes (Mijwel, 2021). The MLP model is a powerful tool for environmental monitoring because of its capacity to serve as a highly flexible function approximator suitable for handling nonlinear and complex properties (Gardner and Dorling, 1998). Consequently, the MLP model has been widely used to estimate ocean salinity (Chen and Hu, 2017; Jang et al., 2022; Kim et al., 2022; Kim et al., 2023a).

To analyze the performance change with the addition of MURSST and HYCOM SSS, three schemes were constructed based on the combination of input variables: Rrs and geolocation (Scheme 1: S1); Rrs, geolocation, and MURSST (Scheme 2: S2); and Rrs, geolocation, MURSST, and HYCOM SSS (Scheme 3: S3).

3.3. Accuracy assessment and model interpretation

The dataset was divided into a training set (1,584,457 samples from 2016 to 2019) and validation set (365,948 samples from 2020) using holdout validation. The slope, coefficient of determination (R^2), root mean square error (RMSE), and bias were used to evaluate the performance of each product.

SHAP analysis was conducted to interpret the contributions of input variables in the machine learning model for SSS estimation. SHAP is one of the XAI techniques based on game theory that measures the contribution of each feature by assuming that predicted values are a linear summation of weighted input variables (Shapley, 1953). Depending on the machine learning algorithm used, an appropriate SHAP algorithm (e.g., tree SHAP, deep SHAP, or kernel SHAP) should be applied (Lundberg and Lee, 2017). In this study, the kernel SHAP, which is universally applicable regardless of the model type, was used to interpret the neural network-based model.

4. Results

4.1. Accuracy assessment

S3 utilized MURSST and HYCOM SSS as input variables, and it showed the best performance among all comparative schemes in the validation using the holdout dataset (Fig. 3). HYCOM SSS tended to slightly overestimate the SSS compared to SMAP SSS-J. The SSS estimation performance improved from the low- to high-salinity range (Table S1). HYCOM SSS demonstrated relatively high accuracy in the high-salinity range, but showed very low accuracy in the nominal- and low-salinity ranges. S1, which used only GOCI Rrs as the input variable, exhibited lower accuracy than HYCOM SSS in the high-salinity range, but significantly higher accuracy in the nominal- and low-salinity ranges. When the additional input variables MURSST and HYCOM SSS were included, the accuracy gradually improved (Figs. 3 (b)–(d) and S1). Consequently, S3 exhibited RMSE values of 0.35, 2.28, and 3.63 psu in the high-, nominal-, and low-salinity ranges, respectively, demonstrating the best performance across all salinity ranges (Table S1).

Validation of SMAP SSS with the in situ datasets (Liu, FEM, SOO, and TSG) showed that SMAP SSS-J performed better overall than SMAP L3 SSS (Fig. 4(a)–(b)). SMAP SSS-J showed a slightly decreased

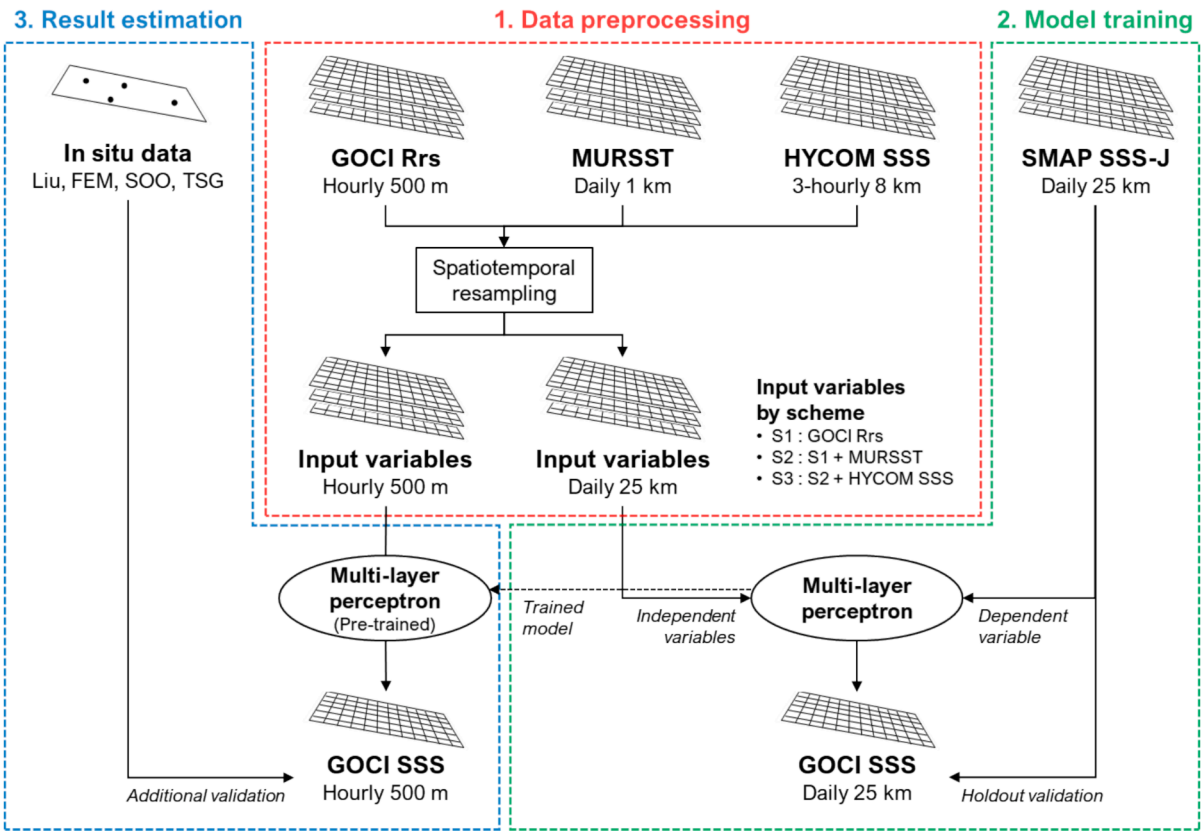

Fig. 2. Research flow diagram of this study. The model was trained at the scale of SMAP SSS-J (daily, 25 km). The final products were retrieved at the scale of GOCI Rrs (hourly, 500 m).

performance in low-salinity regions compared to SMAP L3 SSS, but its performance was significantly better in nominal- and high-salinity regions (Table S2). Compared to the Liu dataset (covering low to high salinity), SMAP SSS-J was slightly less accurate than SMAP L3 SSS. However, the opposite trend was observed when compared with the SOO dataset (covering nominal to high salinity). Notably, when compared with the FEM and TSG datasets (high salinity), SMAP SSS-J significantly outperformed SMAP L3 SSS.

The validation results of the HYCOM SSS and comparative schemes of the GOCI SSS using the in situ dataset showed similar trends to the validation results using the holdout dataset (Figs. 3 and 4(c)–(f)). HYCOM SSS exhibited high accuracy in FEM and TSG, but showed lower accuracy in Liu and SOO (Table S2). Although S1 demonstrated a lower accuracy in FEM and TSG than HYCOM SSS, it was more highly accurate in Liu and SOO. As the number of input variables increased, the accuracy gradually improved, with S3 ultimately showing the best performance among the comparative schemes for all in situ datasets (Figs. 4(d)–(f) and S2). S3 outperformed SMAP SSS-J, which was used as the target data during model training (Fig. 4(b) and (f)).

The MLP S3 model exhibited the best SSS estimation performance, and the impact of each input variable on SSS estimation was analyzed using the model (Fig. 5). The feature importance was found to be the highest for geolocation (latitude and longitude), followed by HYCOM SSS, MURSST, and Rrs. Latitude generally improved model predictions when the feature value was low, but it reduced the predictions when the value was high; longitude showed the opposite trend. However, both features had varying impacts depending on the range of feature values, indicating that their contributions to predictions could change under different conditions. HYCOM SSS generally made strong negative contributions to predictions when the feature value was low, but its contribution was slightly positive when the value was high. MURSST made a negative contribution when the feature value was high and a positive contribution when the value was low, effectively reflecting the seasonal variability of SSS. Among the Rrs bands, Rrs412 had the highest feature importance and generally contributed positively to predictions, aligning with theoretical expectations related to CDOM (Bai et al., 2013; Fournier et al., 2015). However, the remaining Rrs bands had relatively less influence and showed inconsistent contribution patterns, making their relationship to SSS less clear.

4.2. Spatiotemporal pattern in East Asia

SMAP SSS-J and GOCI SSS exhibited similar seasonal patterns in each of the major East Asian Seas (Fig. 6). In the NWP, which is relatively less affected by the CDW, salinity remained consistently high throughout the year, despite a slight decrease in August due to high precipitation. In contrast, the ECS, which is directly affected by the CDW, exhibited relatively low-salinity levels and a distinct seasonal pattern. Particularly in August, when the CDW impact was at its peak, the ECS had the widest low-salinity plume. Both the YS and ES were slightly affected, leading to a decrease in salinity (Fig. 6(c) and (g)).

The intra-monthly variations in the SMAP SSS-J and GOCI SSS were analyzed for August 2020, a period marked by widespread flooding across China (Fig. 7). The heavy rainfall that persisted since June 2020 caused a substantial influx of low-salinity water into the ECS. However, after August 20, typhoons Maysak and Bavi passed through the ECS, mixing low-salinity surface water with high-salinity deep water, thereby weakening the low-salinity plume. Both SMAP SSS-J and GOCI SSS accurately reflected this intra-monthly variation in the CDW. On August 1, low-salinity water formed in the ECS, and it expanded to the South Sea of Korea by August 15, but contracted back to the ECS by August 31 (Fig. 7).

GOCI SSS (500 m) simulated more detailed spatial patterns that were not captured by SMAP SSS-J (25 km); this included ocean phenomena

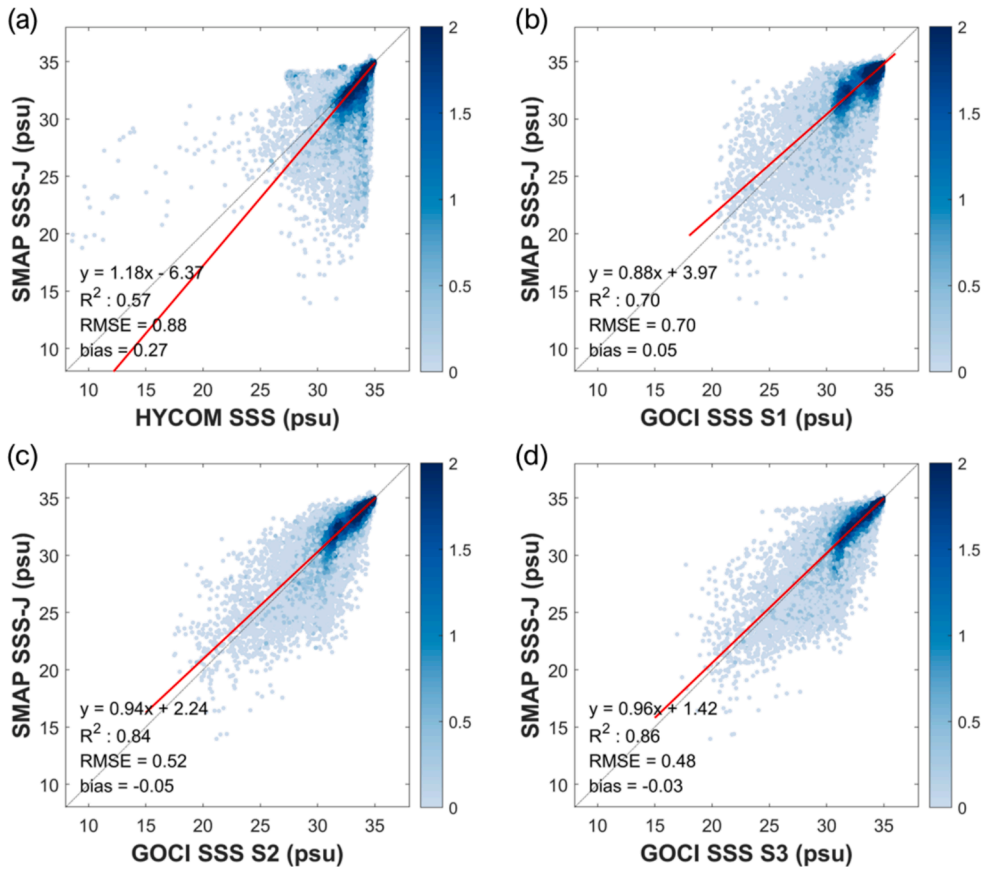

Fig. 3. Scatter plots comparing SMAP SSS-J with (a) HYCOM SSS and (b)–(d) the comparative schemes of GOCI SSS. The Y-axis represents the log scale of data density.

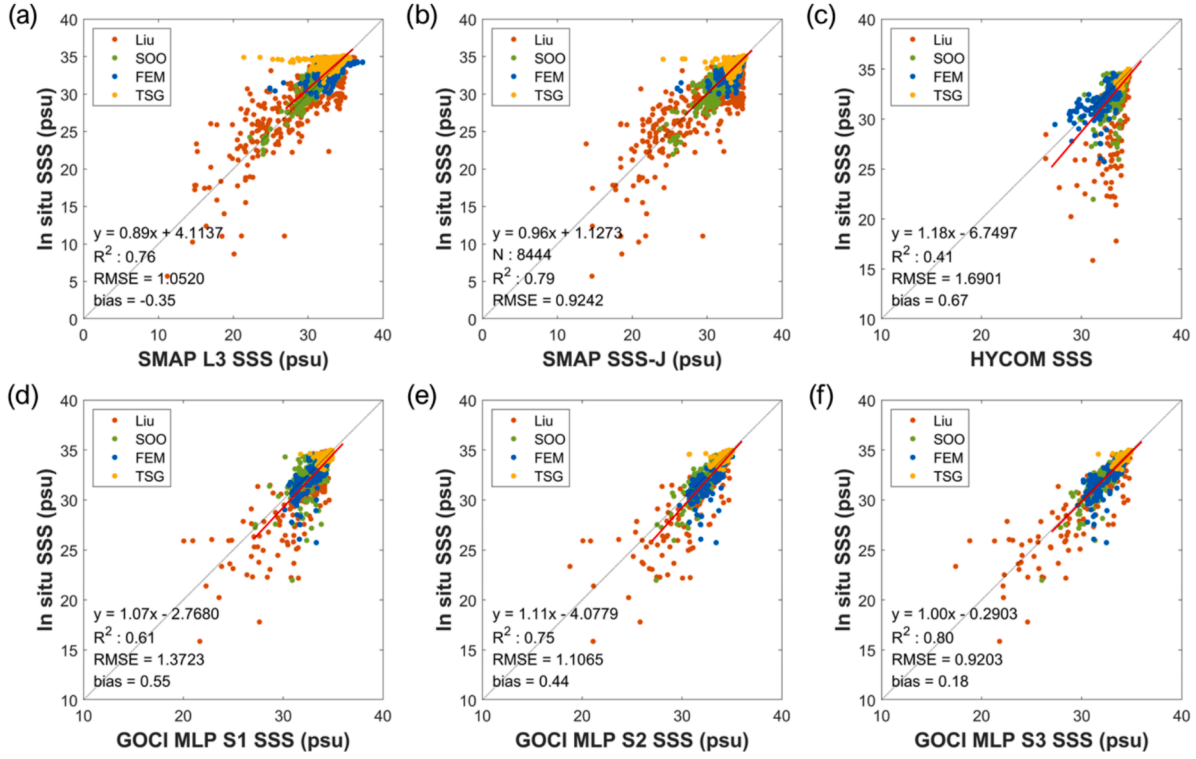

Fig. 4. Scatter plots comparing the in situ dataset with (a) SMAP L3 SSS, (b) SMAP SSS-J, (c) HYCOM SSS, and (d)–(f) comparative schemes of GOCI SSS.

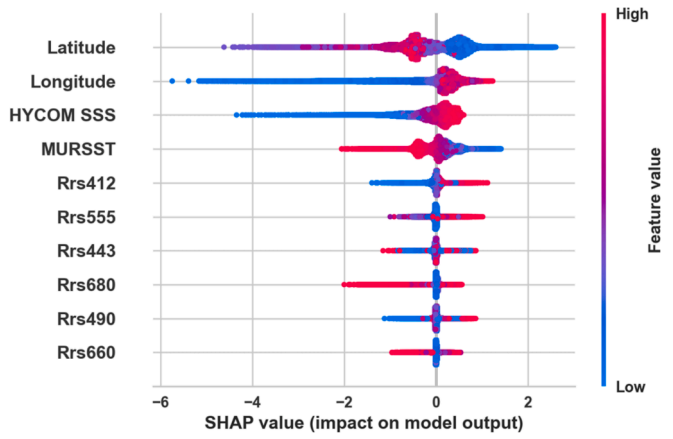

Fig. 5. SHAP summary plot of the MLP S3 model. Each feature is sorted according to the magnitude of its impact on the prediction: the most important features are shown at the top, with less important ones placed below. The feature value represents the actual value of a specific feature, and the SHAP value indicates the degree to which each feature contributes to the prediction.

such as coastal upwelling, which are analyzed in more detail in Section 4.3. Additionally, SMAP SSS-J missed a significant amount of information in coastal seas due to RFI and LC, which are essential for aquaculture fisheries and coastal ecosystem monitoring (Figs. 6(a)–(d) and 7(a)–(c)). GOCI SSS provides high-resolution information on coastal seas where SMAP SSS-J lacks data (Figs. 6(e)–(h) and 7(d)–(f)). However, the GOCI SSS tended to slightly overestimate the SSS in the ECS region compared to the SMAP SSS-J (Fig. 7(b) and (e)). As noted in Section 4.1, the performance of GOCI SSS was slightly poorer in the low-salinity range, with amplified error in summer due to data loss from cloud cover.

The spatial patterns of the SHAP values for each input variable in February (winter dry monsoon) and August (summer wet monsoon) were analyzed (Fig. 8). Both HYCOM SSS and MURSST exhibited significant contributions ($|SHAPvalue| > 0.4$) in various regions depending on the season. HYCOM SSS showed a tendency to reduce model predictions when the feature value was low and improve predictions when the feature value was high, whereas MURSST exhibited the opposite pattern (Figs. 8 (a)–(b), (e)–(f), and S3(a)–(b), (e)–(f)).

For Rrs, moderate contributions ($|SHAPvalue| > 0.2$) were observed only in specific coastal regions, including river-dominated areas in the ECS. Particularly, compared to the winter dry monsoon, the summer wet monsoon's higher rainfall expanded the CDW region, increasing the area contributing to model predictions (Fig. 8(c)–(d) and (g)–(h)). Overall, both Rrs features demonstrated a tendency to reduce model predictions when the feature value was low and improve predictions when the feature value was high (Figs. 8 (c)–(d), (g)–(h), and S3(c)–(d), (g)–(h)). However, for Rrs555, some shallow water regions deviated from this general trend.

The contribution of each input variable varied spatially. In regions where the contribution of one feature was low, another feature often showed a high contribution, indicating that features with different characteristics had complementary relationships. These findings are consistent with the contribution patterns of each feature to the model predictions, as shown in the Fig. 5, and they also align with the spatial distributions of correlations between SMAP SSS-J and input variables (Fig. S4).

4.3. Variations from cold-water mass

In the ES, coastal upwelling frequently occurs along the coastline, transporting cold bottom water to the surface and leading to the frequent formation of cold-water masses during the summer. The cold-water mass is defined as areas with SST at least 5 ℃ lower than the surrounding water, prompting the NIFS to issue advisories. Coastal upwelling transports cold, saline, and nutrient-rich bottom waters to the surface, significantly affecting the marine environment (Han et al., 2016; Kim et al., 2008). Fig. 9 shows the spatial distribution of MURSST, SMAP SSS-J, and GOCI SSS during the period when the cold-water mass advisory was issued in 2020. A cold-water mass was detected on the coastline of the ES (Fig. 9(a) and (d)). Due to the low resolution and high uncertainty in coastal areas, SMAP SSS-J did not show a distinct SSS change (Fig. 9(b) and (e)). In contrast, GOCI SSS detected a slight increase in the SSS distribution near the cold-water mass (Fig. 9(c) and (f)). This finding aligns with previous studies that observed increased SSS during coastal upwelling in the ES (Lee and Kim, 2003; Park and Kim, 2010).

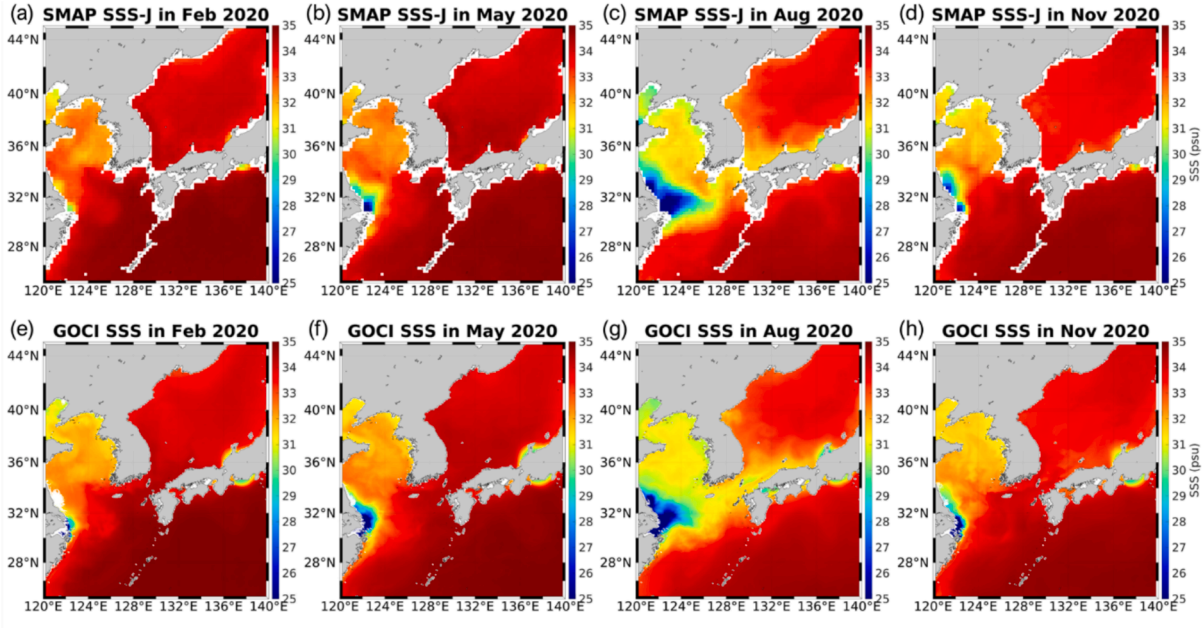

Fig. 6. Spatial distributions of the monthly average (a)–(d) SMAP SSS-J and (e)–(h) GOCI SSS in 2020: (a) and (e) February, (b) and (f) May, (c) and (g) August, and (d) and (h) November.

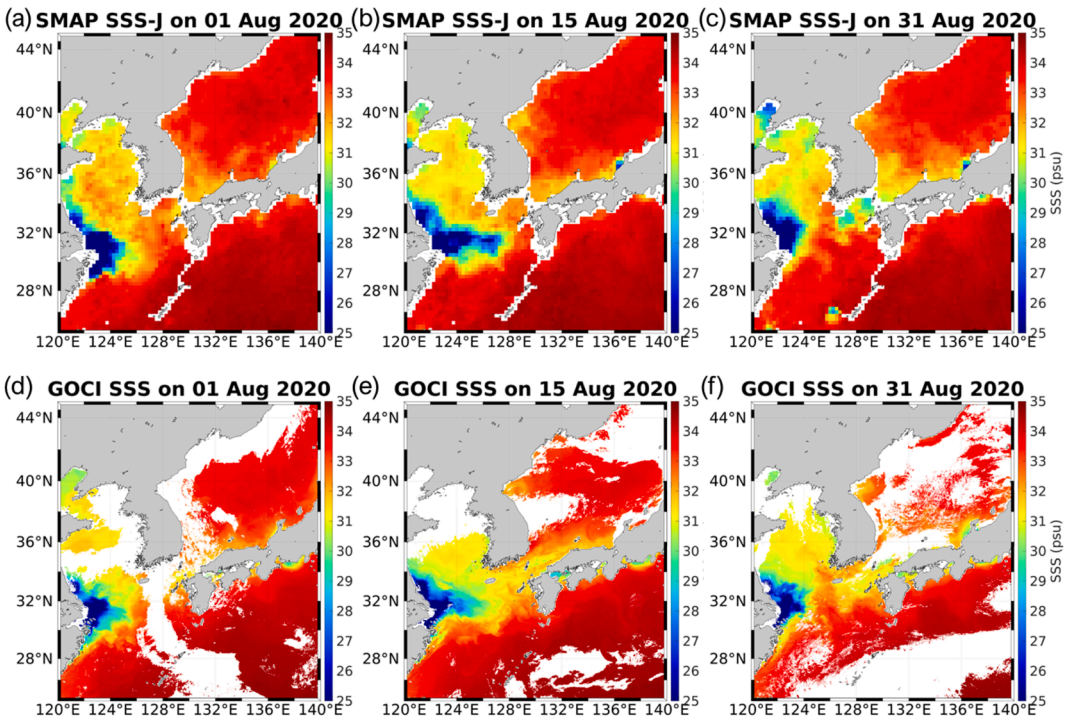

Fig. 7. Spatial distributions of the daily average (a)–(c) SMAP SSS-J and (d)–(f) GOCI SSS in 2020: (a) and (d) 01 August, (b) and (e) 15 August, and (c) and (f) 31 August.

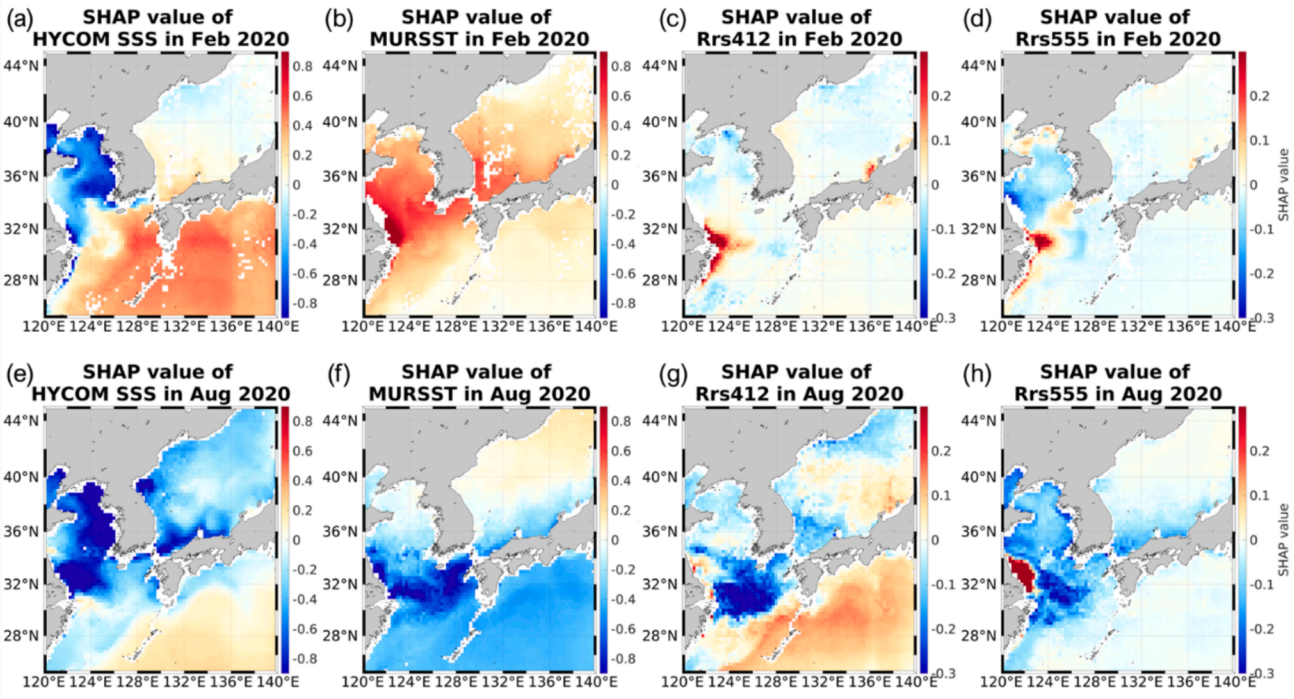

Fig. 8. Spatial distributions of the monthly average SHAP values for each feature in 2020: (a)–(d) February (winter dry monsoon) and (e)–(h) August (summer wet monsoon). (a) and (e) HYCOM SSS, (b) and (f) MURSST, (c) and (g) Rrs412, and (d) and (h) Rrs555.

In the region where the cold-water mass advisory was issued on July 21, 2020, HYCOM SSS and MURSST showed relatively higher feature contributions than Rrs (Fig. 10). HYCOM SSS increased the prediction in areas where its feature values were relatively higher than the surrounding regions, whereas MURSST exhibited the opposite pattern (Figs. 9(a), S5(a), and 10(a)–(b)). The SHAP values of these two features closely matched the spatial patterns of low temperature and high salinity caused by the cold-water mass and were consistent with the SHAP analysis results presented in Sections 4.1 and 4.2 (Figs. 9(a) and (c), and 10(a)–(b)). In contrast, Rrs showed minimal variability in its feature values and did not demonstrate a clear relationship with its contribution to the predictions. (Figs. S5(b)–(c), and 10(c)–(d)).

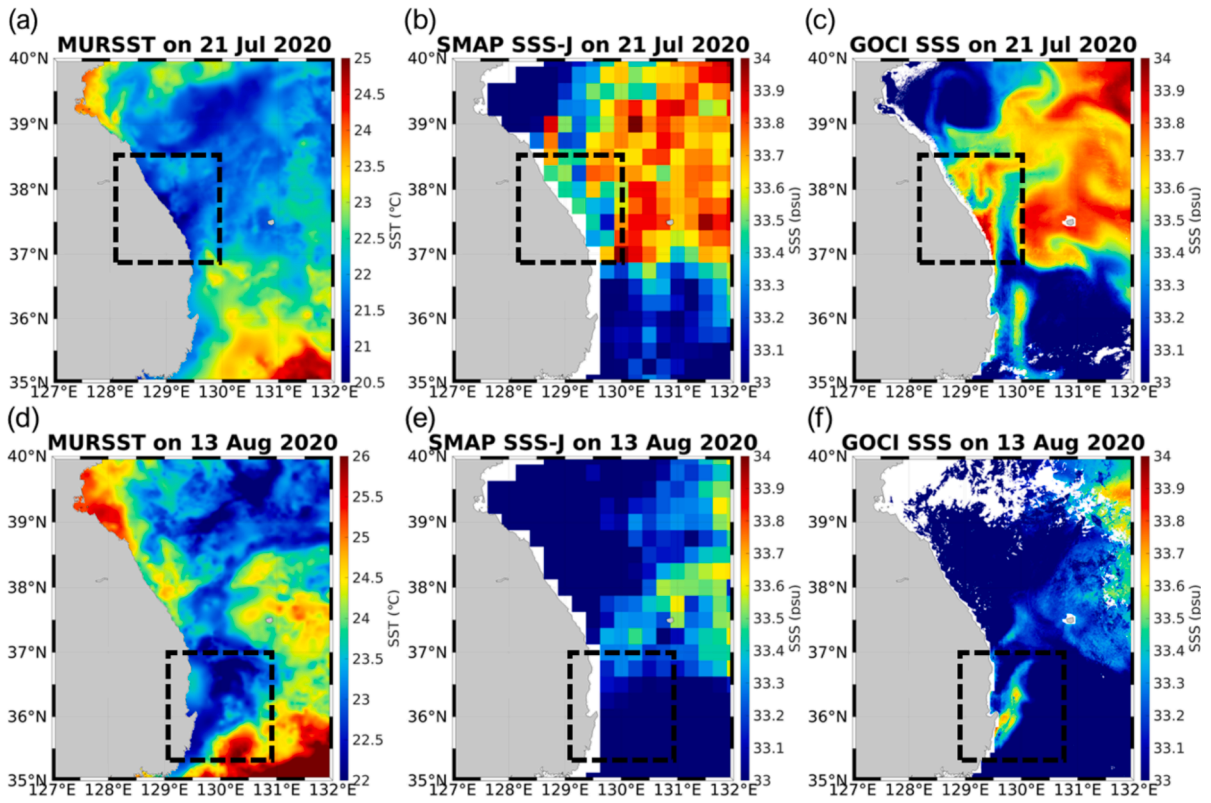

Fig. 9. Spatial distributions of the daily average (a) and (d) MURSST, (b) and (e) SMAP SSS-J, (c) and (f) GOCI SSS in 2020. The dashed black box indicates the region where the cold-water mass alert was issued.

5. Discussion

5.1. Contribution of each feature in coastal seas

Due to the limited characteristics of OC signals, many previous studies have concentrated on specific regions (such as river-dominated areas) or on particular periods (such as the summer wet monsoon), which are heavily influenced by freshwater influx (Kim et al., 2020; Kim et al., 2022; Son and Choi, 2022; Sung et al., 2022). In river-dominated areas, the correlation between OC signals and SSS is most evident in Rrs412, associated with CDOM absorption, and Rrs555, related to TSM scattering. According to previous studies, large amounts of CDOM and TSM flow into the ECS along with low-salinity water during summer, resulting in a positive correlation between Rrs412 and SSS and a negative correlation between Rrs555 and SSS (Kim et al., 2022; Kim et al., 2020). In this study, Rrs412 followed this general trend, but Rrs555 showed a slightly opposite pattern (Figs. 5, 8, S3 and S4).

Low-salinity water in the ECS and YS is affected not only by freshwater influx from rivers, but also by vertical seawater mixing. Vertical mixing increases SSS by mixing low-salinity surface water with high-salinity deep water while also increasing TSM in shallow regions by transporting sediments to the surface. While the SSS variation caused by freshwater influx is limited to the summer season and river-dominated areas, the SSS variation from vertical mixing can occur throughout the ECS and YS, regardless of the season. During summer, the optical properties of the ECS are strongly influenced by organic phytoplankton particles, as the large sediment influx from strong CDW is rapidly deposited due to pronounced stratification, leaving the upper mixed layer dominated by organic materials (Chen et al., 2018; Guo et al., 2023). This is evident from the notably low summer Rrs555 values observed in the region (Fig. S3(h)). Therefore, the correlation between Rrs and SSS presented in previous studies focusing on the summer season is primarily attributed to the influence of organic particles.

Outside summer, the optical properties of the ECS are primarily influenced by vertical mixing and TSM due to its shallow depth (Guo et al., 2023; Mao et al., 2018). Unlike previous studies, this research modeled the entire East Asian seas across all seasons, incorporating SSS changes caused by freshwater influx and vertical mixing into the model. Therefore, the positive correlation between Rrs555 and SSS presented in this study can be attributed to the expanded temporal and spatial scope of the analysis. This conclusion is supported by several findings: the alignment of seasonal patterns of SSS and Rrs555 in the ECS and YS (Figs. 6, S3(d), and (h)), the significant contribution of Rrs555 in relatively shallow regions (Fig. 8(d) and (h)), and the positive correlation between SSS and Rrs555 in these areas (Fig. S4(d)).

5.2. Contribution of each feature in open ocean

This study demonstrates that it is possible to estimate SSS with a high accuracy by combining HYCOM SSS and MURSST with OC signals; this is not only possible in coastal seas (ECS and YS; mainly case 2 water) as explored in previous research, but also in open oceans (ES and NWP; mainly case 1 water). The success in modeling the entire region of East Asia was due to HYCOM SSS and MURSST effectively compensating for the lower contribution of GOCI Rrs in open oceans (Fig. 8). This advantage was particularly evident in the analysis of the cold-water mass in the ES. Case 1 water generally showed less variability in OC signals compared to case 2, with Rrs decreasing from blue to red wavelengths (Kim et al., 2020; Matsushita et al., 2012). In cold-water mass regions, the contribution of Rrs was very low, with Rrs555 showing near-zero feature and SHAP values throughout the ES (Fig. 10 (c)–(d) and S5(b)–(c)). This explains why GOCI SSS S1 struggled to simulate high-salinity patterns (Fig. 3(b) and Table S1), highlighting the limitations of approaches relying on the indirect correlation between Rrs and SSS. In contrast, HYCOM SSS and MURSST showed strong feature contributions, successfully simulating cold-water mass patterns not even

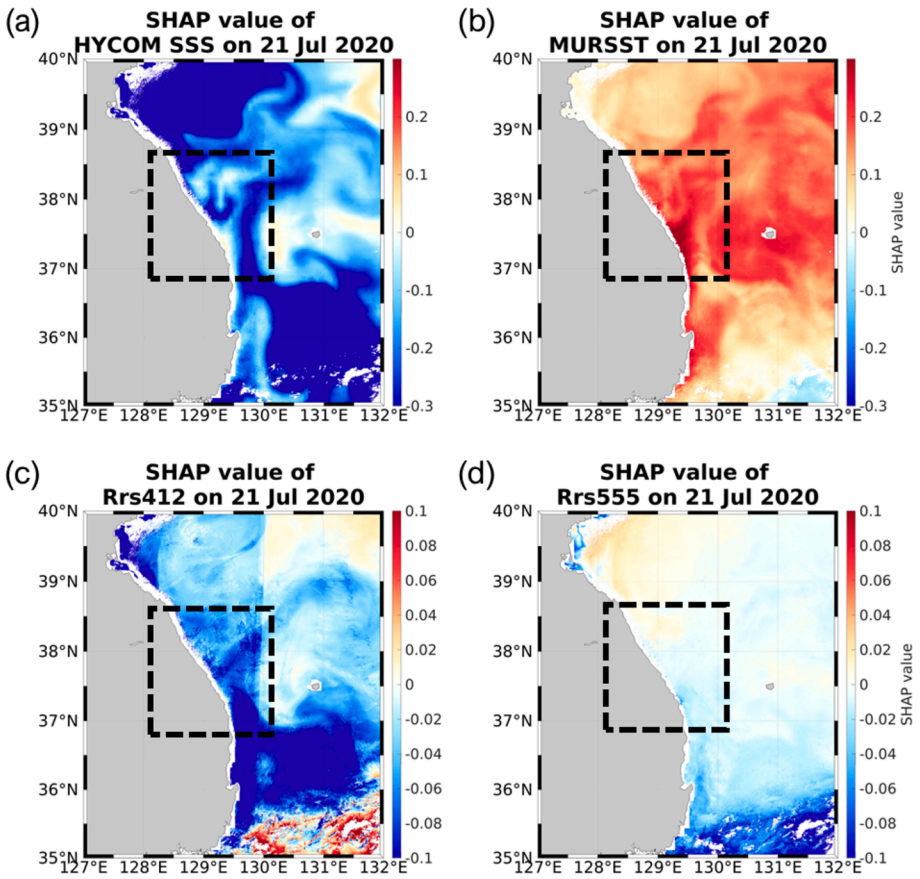

Fig. 10. Spatial distributions of daily average SHAP values for each feature on July 21, 2020: (a) HYCOM SSS, (b) MURSST, (c) Rrs412, and (d) Rrs555. The dashed black box indicates the region where the cold-water mass alert was issued.

observed in the SMAP SSS-J (Fig. 9(a)–(c) and 10(a)–(b)). Due to the high accuracy of HYCOM SSS in these regions, GOCI SSS S3 better-simulated high-salinity patterns compared to other schemes (Fig. 3 and Table S2).

6. Novelty and limitations

While previous studies used SMAP L3 SSS as reference data for training, this study utilized SMAP SSS-J, which is derived from corrected and gap-filled SMAP L2B SSS (Jang et al., 2024; Jang et al., 2022; Kim et al., 2022; Kim et al., 2020; Kim et al., 2023a). This improved dataset enabled us to train the model, demonstrating high accuracy across a wide range of salinity values when validated against field measurements from various sources. Traditionally, OC satellite-based SSS studies have been limited to coastal seas due to the limited correlation between OC signals and salinity (Ahn et al., 2008; Chen and Hu, 2017; Son and Choi, 2022). However, by integrating HYCOM SSS and MURSST as input variables, our approach achieved spatial generalization, extending its accuracy beyond coastal seas and into the open oceans. Specifically, this integration allowed us to capture high-resolution SSS variations, such as those caused by cold-water masses near the coastline of the ES. Previous studies often analyze the relationship between OC signals and SSS using statistical values, whereas this study used SHAP, revealing spatiotemporal variations across broader regions and seasons and offering deeper insights (Kim et al., 2022; Kim et al., 2020; Sung et al., 2022).

Despite these advances, several limitations remain. One challenge is that the missing coastal samples in SMAP SSS-J caused RFI and LC, which prevented sufficient training for coastal areas. Although boundary padding was applied to SMAP SSS-J to reduce missing values compared to the original SMAP data, the coarse spatial resolution (25 km) still resulted in persistent gaps near the coast. Additionally, the inability to retrieve SSS in cloud-covered areas (an inherent limitation of optical satellites) may have influenced the results. This issue is particularly relevant in the study area, where cloud cover varies significantly by season and region. Furthermore, the reliance on satellite and numerical model data for continuous spatiotemporal analysis introduces uncertainties. Improving the atmospheric correction algorithm of GOCI in coastal areas is especially important for enhancing the accuracy in these regions (Liu and Wang, 2024). These limitations highlight the need for further research to address and mitigate these challenges.

7. Conclusion

In this study, a high-resolution SSS estimation model with high accuracy in both coastal seas and open oceans was developed by integrating multi-source data. The MLP S3 model, which uses GOCI Rrs, MURSST, and HYCOM SSS as input variables, outperformed the S1 model, which uses only GOCI Rrs, and the S2 model (using both GOCI Rrs and MURSST). Furthermore, its performance was better than that of both SMAP SSS-J and HYCOM SSS. The GOCI SSS simulated the spatiotemporal patterns of low-salinity in coastal seas and open oceans in East Asia, similar to SMAP SSS-J, but with a higher resolution. In the ES, it reproduced salinity changes caused by cold-water masses not captured by SMAP SSS-J, taking advantage of auxiliary variables. SHAP analysis revealed that the contributions of each feature in the East Asian seas varied by season and region. They compensated for each other's lower contributions, resulting in a complementary effect. Unlike previous studies that focused on the wet summer monsoon period and river-dominated areas, this study analyzed SSS patterns due not only to freshwater runoff from rivers, but also vertical seawater mixing,

covering a wider region and all seasons. In conclusion, by integrating features with diverse characteristics, we demonstrated that SSS estimation over a broader region and longer periods is possible, revealing new salinity patterns not addressed in previous research. These findings have important implications for marine environmental studies and predictive modeling.

CRediT authorship contribution statement

Taejun Sung: Writing – original draft, Visualization, Validation, Methodology, Investigation, Formal analysis, Conceptualization. **So-Hyun Kim:** Writing – original draft, Visualization, Validation, Methodology, Investigation, Formal analysis, Conceptualization. **Seongmun Sim:** Writing – review & editing, Investigation, Data curation. **Daehyeon Han:** Writing – review & editing, Investigation, Data curation. **Eunna Jang:** Writing – review & editing, Data curation. **Jungho Im:** Writing – review & editing, Supervision, Resources, Methodology, Funding acquisition, Conceptualization.

Declaration of competing interest

The authors declare that they have no known competing financial interests or personal relationships that could have appeared to influence the work reported in this paper.

7. Acknowledgement

This research was supported by the Korea Institute of Marine Science & Technology (KIMST), funded by the Ministry of Oceans and Fisheries, under the projects “Development of risk managing technology tackling ocean and fisheries crisis around Korean Peninsula by Kuroshio Current (RS-2023-00256330)” and “Development of technology using analysis of ocean satellite images (RS-2021-KS211406).” S. Kim was partially supported by the Basic Science Research Program through the National Research Foundation of Korea (NRF), funded by the Ministry of Education (RS-2024-00408299).

Appendix A. Supplementary data

Supplementary data to this article can be found online at https://doi.org/10.1016/j.jag.2025.104427.

Data availability

Data will be made available on request.

References

Ahn, Y., Shanmugam, P., Moon, J., Ryu, J.-H., 2008. Satellite remote sensing of a low-salinity water plume in the East China Sea. Annales Geophysicae. Copernicus Publications Göttingen, Germany, pp. 2019–2035.
Bai, Y., Pan, D.L., Cai, W.J., He, X.Q., Wang, D.F., Tao, B.Y., Zhu, Q.K., 2013. Remote sensing of salinity from satellite-derived CDOM in the Changjiang River dominated East China Sea. J Geophys Res-Oceans 118, 227–243.
Barale, V., Gower, J.F., Alberotanza, L., 2010. Oceanography from space: revisited. Springer Science & Business Media.
Chassignet, E.P., Hurlburt, H.E., Smedstad, O.M., Halliwell, G.R., Hogan, P.J., Wallcraft, A.J., Baraille, R., Bleck, R., 2007. The HYCOM (HYbrid Coordinate Ocean Model) data assimilative system. Journal of Marine Systems 65, 60–83.
Chen, S., Zhang, T., Hu, L., Xue, C., Wu, X., 2018. Vertical variations in optical properties of the waters in the Yellow Sea and Bohai Sea at seasonal scales and their influencing mechanisms. Optics Express 26, 4112–4134.
Chen, S.L., Hu, C.M., 2017. Estimating sea surface salinity in the northern Gulf of Mexico from satellite ocean color measurements. Remote Sensing of Environment 201, 115–132.
Chin, T.M., Vazquez-Cuervo, J., Armstrong, E.M., 2017. A multi-scale high-resolution analysis of global sea surface temperature. Remote Sensing of Environment 200, 154–169.
Choi, J.K., Son, Y.B., Park, M.S., Hwang, D.J., Ahn, J.H., Park, Y.G., 2021. The Applicability of the Geostationary Ocean Color Imager to the Mapping of Sea Surface Salinity in the East China Sea. Remote Sensing 13, 2676.
Cummings, J.A., Smedstad, O.M., 2013. Variational data assimilation for the global ocean, Data assimilation for atmospheric, oceanic and hydrologic applications (Vol. II). Springer, pp. 303-343.
Dorfschäfer, G., Tanajura, C., Costa, F., Santana, R., 2020. A new approach for estimating salinity in the southwest atlantic and its application in a data assimilation evaluation experiment. Journal of Geophysical Research: Oceans 125, e2020JC016428.
Fore, A.G., Yueh, S.H., Tang, W.Q., Stiles, B.W., Hayashi, A.K., 2016. Combined Active/Passive Retrievals of Ocean Vector Wind and Sea Surface Salinity With SMAP. Ieee Transactions on Geoscience and Remote Sensing 54, 7396–7404.
Fournier, S., Chapron, B., Salisbury, J., Vandemark, D., Reul, N., 2015. Comparison of spaceborne measurements of sea surface salinity and colored detrital matter in the Amazon plume. J Geophys Res-Oceans 120, 3177–3192.
Gardner, M.W., Dorling, S.R., 1998. Artificial neural networks (the multilayer perceptron) - A review of applications in the atmospheric sciences. Atmospheric Environment 32, 2627–2636.
Guo, J.T., Pan, H.D., Cao, R.C., Wang, J.F., Lv, X.Q., 2023. Multiple Timescale Variations in Water Transparency in the Eastern China Seas over the Period 1997-2019. J Geophys Res-Oceans 128, e2022JC019170.
Han, I.-S., Park, M.-H., Min, S.-H., Kim, J.-Y., 2016. Spatio-temporal variation of cold water masses along the eastern coast of Korea in 2013 and 2014. Journal of the Korean Society of Marine Environment & Safety 22, 286–295.
Jang, E., Han, D., Im, J., Sung, T., Kim, Y.J., 2024. Deep learning-based gap filling for near real-time seamless daily global sea surface salinity using satellite observations. International Journal of Applied Earth Observation and Geoinformation 132, 104029.
Jang, E., Kim, Y.J., Im, J., Park, Y.G., 2021. Improvement of SMAP sea surface salinity in river-dominated oceans using machine learning approaches. Giscience & Remote Sensing 58, 138–160.
Jang, E., Kim, Y.J., Im, J., Park, Y.G., Sung, T., 2022. Global sea surface salinity the synergistic use of SMAP satellite and HYCOM data based on machine learning. Remote Sensing of Environment 273, 112980.
Jin, X., He, X., Bai, Y., Wang, D., Zhu, Q., Gong, F., Pan, D., 2021. Enhancing Spatial Resolution of Sea Surface Salinity in Estuarine Regions by Combining Microwave and Ocean Color Satellite Data. IEEE Geoscience and Remote Sensing Letters 19, 1–5.
Kim, D., Choi, S.H., Kim, K.H., Shim, J., Yoo, S., Kim, C.H., 2009. Spatial and temporal variations in nutrient and chlorophyll-concentrations in the northern East China Sea surrounding Cheju Island. Continental Shelf Research 29, 1426–1436.
Kim, D.W., Kim, S.H., Baek, J.Y., Lee, J.S., Jo, Y.H., 2022. GOCI-II based sea surface salinity estimation using machine learning for the first-year summer. International Journal of Remote Sensing 43, 6605–6623.
Kim, D.W., Park, Y.J., Jeong, J.Y., Jo, Y.H., 2020. Estimation of Hourly Sea Surface Salinity in the East China Sea Using Geostationary Ocean Color Imager Measurements. Remote Sensing 12, 755.
Kim, K., Chang, K.I., Kang, D.J., Kim, Y.H., Lee, J.H., 2008. Review of recent findings on the water masses and circulation in the east sea (Sea of Japan). Journal of Oceanography 64, 721–735.
Kim, S.-H., Kim, D.-W., Jo, Y.-H., 2023a. GOCI-II based low sea surface salinity and hourly variation by typhoon Hinnamnor. Korean Journal of Remote Sensing 39, 1605–1613.
Kim, Y.J., Han, D., Jang, E., Im, J., Sung, T., 2023b. Remote sensing of sea surface salinity: challenges and research directions. Giscience & Remote Sensing 60, 2166377.
Klein, L., Swift, C., 1977. An improved model for the dielectric constant of sea water at microwave frequencies. IEEE Transactions on Antennas and Propagation 25, 104–111.
Kolodziejczyk, N., Hamon, M., Boutin, J., Vergely, J.L., Reverdin, G., Supply, A., Reul, N., 2021. Objective Analysis of SMOS and SMAP Sea Surface Salinity to Reduce Large-Scale and Time-Dependent Biases from Low to High Latitudes. Journal of Atmospheric and Oceanic Technology 38, 405–421.
Lee, T.-S., Kim, I.-N., 2003. Chemical imprints of the upwelled waters off the coast of the southern East Sea of Korea. Journal of the Korean Society of Oceanography 38, 101–110.
Liu, J., Bellerby, R.G.J., Zhu, Q., Ge, J.Z., 2023. Estimating Sea Surface Salinity in the East China Sea Using Satellite Remote Sensing and Machine Learning. Earth and Space. Science 10, e2023EA003230.
Liu, X.M., Wang, M.H., 2024. Improving GOCI ocean color data under high solar-zenith angle over open oceans using neural networks. Giscience & Remote Sensing 61, 2353426.
Lundberg, S.M., Lee, S.I., 2017. A Unified Approach to Interpreting Model Predictions. Advances in Neural Information Processing Systems 30 (Nips 2017) 30.
Mao, Y., Wang, S., Qiu, Z., Sun, D., Bilal, M., 2018. Variations of transparency derived from GOCI in the Bohai Sea and the Yellow Sea. Opt Express 26, 12191–12209.
Martin, S., 2014. An introduction to ocean remote sensing. Cambridge University Press.
Matsushita, B., Yang, W., Chang, P., Yang, F., Fukushima, T., 2012. A simple method for distinguishing global Case-1 and Case-2 waters using SeaWiFS measurements. Isprs Journal of Photogrammetry and Remote Sensing 69, 74–87.
Mijwel, M.M., 2021. Artificial neural networks advantages and disadvantages. Mesopotamian Journal of Big Data 2021, 29–31.
Park, K.A., Kim, K.R., 2010. Unprecedented coastal upwelling in the East/Japan Sea and linkage to long-term large-scale variations. Geophysical Research Letters 37.
Qing, S., Zhang, J., Cui, T.W., Bao, Y.H., 2013. Retrieval of sea surface salinity with MERIS and MODIS data in the Bohai Sea. Remote Sensing of Environment 136, 117–125.
Shapley, L.S., 1953. A value for n-person games.
Shi, W., Wang, M., 2024. Monitoring the Amazon River plume from satellite observations. Giscience & Remote Sensing 61, 2416725.

Son, Y.B., Choi, J.K., 2022. Mapping the Changjiang Diluted Water in the East China Sea during summer over a 10-year period using GOCI satellite sensor data. Frontiers in Marine Science 9, 1024306.
Stogryn, A., 1971. Equations for calculating the dielectric constant of saline water (correspondence). IEEE Transactions on Microwave Theory and Techniques 19, 733–736.
Sung, T., Sim, S., Jang, E., Im, J., 2022. Estimation of high resolution sea surface salinity using multi satellite data and machine learning.
Wei, J.W., Lee, Z.P., Shang, S.L., 2016. A system to measure the data quality of spectral remote-sensing reflectance of aquatic environments. J Geophys Res-Oceans 121, 8189–8207.
Wilson, E.A., Riser, S.C., 2016. An Assessment of the Seasonal Salinity Budget for the Upper Bay of Bengal. Journal of Physical Oceanography 46, 1361–1376.
Woo, H.J., Park, K.A., 2020. Inter-Comparisons of Daily Sea Surface Temperatures and In-Situ Temperatures in the Coastal Regions. Remote Sensing 12, 1592.
Yoon, H., Nam, K., Cho, H., Beun, H., 2004. Study on monitoring and prediction for the red tide occurrence in the middle coastal area in the South Sea of Korea II. The relationship between the red tide occurrence and the oceanographic factors. Journal of Korea Institute of Information and Communication Engineering 8, 938–945.
Zamudio, L., Metzger, E.J., Hogan, P., 2011. Modeling the seasonal and interannual variability of the northern Gulf of California salinity. J Geophys Res-Oceans 116.